Molecules Under Pressure: The Case of [n]Cycloparaphenylenes

Molecules Under Pressure: The Case of [n]Cycloparaphenylenes

Miriam Peña-Alvarez*[1,2,a], Lili Qiu*[3,a], Valentín G. Baonza[1], Mercedes Taravillo[1], Miklos Kertesz[*3] and Juan Casado[*4]

[1]*MALTA-Consolider Team, Department of Physical Chemistry I, Chemistry Faculty, University Complutense of Madrid, 28040 Madrid, Spain.*

[2] Centre for Science at Extreme Conditions, The University of Edinburgh, King's Buildings, Edinburgh, UK.

[3]*Department of Chemistry and Institute of Soft Matter, Georgetown University, 37th and O Streets, NW, Washington, D.C., 20057-1227, USA.*

[4]*Department of Physical Chemistry, University of Málaga, CEI Andalucía Tech, Campus de Teatinos s/n, 29071-Málaga, Spain.*

[a] These authors contributed equally to this work.

e-mail: miriam.pena.alvarez@gmail.com, lq35@georgetown.edu, casado@uma.es, kertesz@geogetown.edu

Abstract. High pressures in the 0-10 GPa range cause molecules to deform in unusual ways. A series of precisely defined carbon nanohoops consisting of *n* para-linked phenyl groups, [n]-cycloparaphenylenes ([n]CPPs, n=7, 8, 9, 10, and 12) were studied in this pressure range using Raman spectroscopy and Density Functional Theory (DFT), and compared with more rigid smaller 5- and [6]CPPs and with the longer carbon nanotubes. The presented analysis sheds light on the different responses to pressure depending on the nanohoop size. Surprisingly, the pressure coefficients, the rate of the Raman shifts as a function of pressure, change at a particular pressure which is characteristic of each [n]CPP. We identified this pressure as the beginning of ovalization of the nanohoops in analogy to carbon nanotubes. This pressure induced ovalization is reversible in the range of pressure studied for [n]CPPs with n=7, 9, 10, and 12. In the case of [8]CPP, we find a metastable conformation at 8 GPa with significantly changed dihedral angles of adjacent phenyls. This high pressure molecular phase of [8]CPP provides an example for a new mechanism of irreversibility involving different conformations upon high pressure treatment. Modeling provided atomic level insights into the changes of conformations and the development of aromatic vs quinonoid structures as a function of pressure.

π-Conjugated molecules undergo a wide variety of transformations under high pressure (such as unusual formation of aggregates and polymers),[1,2] an area of underexplored chemistry mostly due to the difficulties of *in situ* characterization.[3] Of the known cases, benzene undergoes intermolecular bond formation at about 20 GPa forming a surprising polymeric phase.[4, 5, 6] Another example is the fluorene molecule ($C_{13}H_{10}$) which changes its herringbone structure at about 3.6 GPa towards π-stacking, yet no intermolecular bond formation was observed up to 14 GPa.[7] For biscarbonyl[14]annulene, a Hückel aromatic molecule, while a significant reduction of aromaticity occurs under pressure, no intermolecular bond formation was observed up to 9.5 GPa.[8]

As revealed by the cases of benzene, biscarbonyl[14]annulene, and fluorene, due to the malleability of the π–bonds, π–conjugated molecules represent the prototypical niche of compounds where effects of high pressure on the transformation of molecules can lead to a rich diversity of products. Recently we have been interested in π–conjugated cycloparaphenylenes, abbreviated as [n]CPPs and illustrated for n=10 in Figure 1, where *n* represents the number of repeating phenyl units in the nanohoop. The unusual cyclic molecular symmetry of [n]CPPs offers a unique case of cyclic circulation of the π–electron density, or cyclic π–conjugation, which confers on them distinct optical and electronic properties governed by their increasing strain with decreasing *n*.[9] The π–conjugated scientific community has been captivated by the circular aromaticity of [n]CPPs, their tunable size, varying degrees of aromaticity, unique size-dependent supramolecular properties, encapsulation of guest molecules and promising applications in material science.[10,11]

Because [n]CPPs represent the shortest segments of armchair single wall carbon nanotubes (SWCNTs)[12], they can also serve as model systems not only to conceive the bottom-up synthesis of SWCNTs but also to elucidate the nature of the interaction of the nanotube host with guests, as well as other interesting properties.[13,14,15] Since the first synthesis of [n]CPPs (n=9, 12, and 18) in 2008, [16] the family of [n]CPPs was quickly expanded to include the n=5-16, and 18 members of the series and diversified into other functionalized derivatives using various synthetic methods.[16,17,18,,19]

Many different aspects of the *ambient pressure* chemistry of [n]CPPs have been already addressed in different laboratories.[20] From our side, we have initiated a journey into the elucidation of the *high pressure* chemistry and properties of [n]CPPs devoted to the two smallest and highly strained individual members of the series, [5]CPP[21] and [6]CPP.[22] These,

due to their large molecular strain required to close the nanohoops, display a different behavior that cannot be easily fitted into the general trends of larger [n]CPPs. Therefore, now, we report a complete and comprehensive joint analysis of the mechanochemical properties of the [n]CPP series including the larger and thus softer members of the series, those with n=7, 8, 9, 10, and 12 by combining spectroscopy with theory and by putting their singular properties into a common scenario in order to gain insights into the emerging features at high pressure. This will be carried out by monitoring the structures and Raman spectra during pressure cycling. Raman spectroscopy is a widely used tool for the characterization of carbon-based materials in a variety of *in situ* conditions, from which a unique palette of structural–spectroscopic correlations has been established.[23] It is well known that under pressures in the range 5-20 GPa, π–conjugated molecules can form σ–bonded aggregates, hence we will emphasize the nature and size-dependent propensity of [n]CPPs to deform existing bonds or to form new ones and will relate the pressure effects to their molecular shapes and electronic properties (i.e., inter-benzene conformations and tuned aromaticity in the benzene rings that constitute CPPs).

The mechanical responses of SWCNTs have been widely studied and it is well known that along their long dimension they are among the strongest existing materials.[24,25] However, SWCNTs are softer in the cross sectional directions, and for those with large diameters even collapsed peanut shaped configurations have been indicated.[26,27,28] Even at ambient pressures some deviations from the perfect cylindrical shape for larger diameter nanotubes have been noted.[29] It has been suggested that SWCNTs undergo structural transitions during compression with cross sectional changes from circular to oval and then to peanut shapes.[30,31] Such anisotropy thus fundamentally influences the electronic and mechanical properties of SWCNTs.[32,33,34] In these studies, pressure-dependent Raman experiments have provided essential information about their mechanical properties.[35,36] Since pressure displaces the equilibrium geometry into the repulsive part of the anharmonic energy-deformation coordinate function, the pressure-dependent Raman frequencies provide key information about mechanical properties beyond the linear elastic regime, as it has been shown for CNTs.[35,36] The pressure at which SWCNTs become appreciably oval has been defined as the ovalization pressure, P_{oval}. Given that the selective synthesis of SWCNTs with specific diameters is still not sufficiently optimized, there are few high-pressure experimental works which studied their properties with the diameter as a structural variable.[37] Consequently, given the precisely defined molecular structures of [n]CPPs, these molecules can provide valuable answers by the precise elucidation of their high pressure properties in connection with those of SWCNTs.

In this paper we carry out the following analysis, such as outlined in Figure 1: i) the study of the mechanical, structural, and chemical properties of [n]CPPs under high pressure; ii) the comparison of the behavior of [n]CPPs with those known for SWCNTs; iii) the theoretical simulation of high pressure conditions which will give accesses to molecular and electronic properties as a function of pressure in order to guide and help to explain the experimental spectroscopic findings; and iv): we compare the high pressure behaviors of the less strained [n]CPPs (with n>6) with the most highly strained two members of the group (n=5, and 6).

RESULTS AND DISCUSSION

1 Vibrational Raman spectra: General insights of the dependence with pressure. There is a common Raman response that reveals structural ovalization of CNTs consisting of a sudden change of the rate of frequency shift as a function of pressure ($\Delta\nu_i/\Delta P$, pressure coefficients where *i* refers to the *i*-th normal mode) that occurs at the same pressure for all modes, a critical pressure termed as ovalization pressure which is of key importance in this work. This effect is especially noticeable for the CC stretches, the so called "G" modes of CNTs. [38,39,40,41] The second most significant spectral signature related to the deformation of CNTs upon pressure is the disappearance of Raman bands due to the radial breathing modes. [41,42] In this paper, we will study the $\Delta\nu_i/\Delta P$ coefficients at pressures below and above the ovalization pressure, referred as $S_{1,i}$ and $S_{2,i}$, respectively.

Figure 2 shows the Raman spectra of [n]CPPs, n=7-10 and 12 at selected pressures. We divide their analysis into three regions for which the most intense bands are discussed. Their assignments at P=0.1 MPa are given in Table S1.

1A The 1600 cm^{-1} wavenumber region. We mainly focus the discussion on the G_{A1g} and G_{E2g} bands around 1580 cm^{-1} related to the collective CC stretching modes.[43,44] These modes provide information on π-electron delocalization and aromaticity. A general observation is that all Raman bands upshift with increasing pressure.

1B The 1250 cm^{-1} wavenumber region. Around 1250 cm^{-1} we observe five sub-bands resulting from different vibrational combinations of phenyl breathing modes, CC stretching modes, and CH waging bending modes. For simplicity, we will refer to these as the 1190, 1200, 1250, 1280, and 1290 cm^{-1} bands which. also significantly broaden upon compression thus hindering the analysis of their possible resolution into sub-bands at higher pressures.

1C The 100-1200 cm^{-1} wavenumber region. Several bands in this region are assigned either as CCC bending modes or radial flexural modes, in addition to the typical pseudo radial breathing modes and the radial breathing modes, p-RBM and RBM, respectively).[43,44] In line with the findings in CNTs, the p-RBM intensity decays with increasing pressure for all [n]CPPs. The new information here is that since in [n]CPPs the p-RBM bands are measured in out-of-resonant conditions, their intensity decays as the result of an intrinsic increase of fluorescence/reabsorption during compression, and not due to resonance effects.

2 Variable pressure Raman shifts: Theoretical insights and discussions of the $\Delta\nu_i/\Delta P$ pressure coefficients. Our experimental results are accounted for and supported by quantum chemical calculations conducted under simulation of hydrostatic high pressure. Figure 3 represents the pivotal experimental-versus theoretical comparison of the pressure dependence of the different Raman bands for each [n]CPP. In all systems from [7]- to [12]CPP, the G_{A1g} - G_{E2g} and the 1250 cm^{-1} bands show a general upshift with positive pressure coefficients for most of the Raman bands, seen both in the experiments and computations. These $S_{1,i}$ and $S_{2,i}$ pressure coefficients follow that $S_{1,i} > S_{2,i}$.

This pressure-dependent Raman behavior has been already established for the G bands of CNTs from which we know that the ovalization pressure (P^n_{oval}) strongly depends on the diameter of the CNTs.[45] Eq. (1) describes approximate piecewise linear trends, postulating that the pressure at which the rate changes for each *n* is a shared parameter for all vibrational frequencies. In what follows, in analogy with CNTs, we will discuss P^n_{oval} as a characteristic parameter. The formulas are:

$$\omega_i(P)=\omega_i(0)+S_{1,i}P, \text{ if } (P< P^n_{oval}) \quad (1a)$$

$$\omega_i(P)=\omega_i(0)+S_{1,i}P^n_{oval}+S_{2,i}(P-P^n_{oval}), \text{ if } (P>P^n_{oval}), \quad (1b)$$

where $S_{1,i}$ and $S_{2,i}$ correspond to the pressure coefficients at pressures below and above P^n_{oval} respectively, and $\omega_i(0)$ is the Raman shift at ambient pressure. Then, for each band we have

three parameters ($\omega_i(0)$, $S_{1,i}$, $S_{2,i}$) for a given *n*. Note that the P_{oval}^{n} parameter is independent of the band index *i* and is unique for each [n]CPP.

The $S_{1,i}$ and $S_{2,i}$ pressure coefficients for the G_{A1g} and G_{E2g} bands as a function of *n* are shown in Figures 4a and 4b, respectively. Large positive pressure coefficients for a Raman band are correlated with large structural deformations along the vibrational displacement defined by the given normal mode. All $S_{1,i}$ and $S_{2,i}$ values for the G modes show a good agreement between calculations and experiments, and between these, in general, the coefficients of the G_{A1g} mode is found experimentally to be lower than the G_{E2g} coefficient. For both G modes, there is a clear relationship between the pressure coefficients and *n*, with larger values corresponding to larger *n*. The detailed numerical values of the $S_{1,i}$ and $S_{2,i}$ experimental and computed pressure coefficients below and above the ovalization pressure for each G and 1250 bands are summarized in Table S2 and Figure S2 (see Figure S3-S8 and Table S3-S5 for the analysis of the Raman shift of lower frequency modes and RBMs).

Comparing Figures 4a and 4b, one can observe a significant decrease passing from $S_{1,i}$ to $S_{2,i}$ for most Raman bands, with $S_{1,i}$ being typically about twice as large as $S_{2,i}$. In simple terms, why is $S_{1,i} > S_{2,i}$ for most Raman bands and for all [n]CPPs? Similar mode softening ($S_{1,i} > S_{2,i}$) of three intense Raman active bands with increasing pressure have been observed for poly-paraphenylene.[46] A mixed trend with some pressure coefficients are increasing while others are decreasing with increasing pressure was observed also for linear oligo-paraphenylenes[47,48] and for SWCNTs[38,39,40,41,49]. This effect is to a large extent due to the fact that different normal modes are affected differently by pressure induced deformations. Among others, Sun et al.[26] find for (10,10) SWCNT a softening of the G bands ~1 GPa which they relate with the ovalization of the tube. Peters et al.[38] attributed the sudden decrease of the Raman pressure coefficient at 1.7 GPa for (10,10) and (17,0) SWCNTs also to such a softening deformation with increasing pressure. The presented $S_{1,i} > S_{2,i}$ trend as observed for most bands of most [n]CPPs is in line with the interpretation of an ovalization (rigid-to-soft) transition in analogy with the SWCNTs. The rigid-to-soft transition can be understood by the fact that below P_{oval}^{n} pressure will cause the shrinking of the tube, while at pressures above P_{oval}^{n}, tubes are softer in the minor axis direction after ovalization.

We have compared the $S_{1,i}$ values obtained for [n]CPPs with those of SWCNTs from the literature and for the related linear oligo-paraphenylenes in Figure S2: [n]CPPs and SWCNTs follow a parallel trend and, as already noted, $S_{1,i}$ rapidly grows when the number of

phenyl units increases, a spectroscopic feature exclusively related to the larger diameter of the nanohoops similar to the trends in nanotubes. A new peak observed for [7]CPP around 1605 cm^{-1} (shown in orange in Figure 2) is well reproduced by quantum chemical calculations at high pressures. This mode emerges from the band splitting of the G_{E2g} mode as the symmetry is reduced from circular to oval. This splitting of the G_{E2g} mode is also reproduced theoretically for the other [n]CPPs although it is not experimentally detected, likely due to spectral broadening.

The right two columns in Figure 3 show the pressure responses of the five bands near 1250 cm^{-1} for the different [n]CPPs. There is a good agreement between the calculated and experimental $S_{1,i}$ and $S_{2,i}$ values. The broadening of the bands is mirrored the quantum chemical calculations that predict band splittings due to the reduction of symmetry at high pressures. Similarly to the G bands, these trends also display an approximately linear relationship between upshift and increasing pressure with the rates changing at around the same P_{oval}^{n} values for each *n*. These Raman bands are the combination of CC and CH bending modes, and consequently, the change in the rate might be ascribed to changes in torsions as ovalization develops.[43,44] In addition, as shown in Figure 3, Table S1, and Figure S1, the $S_{1,i}$ and $S_{2,i}$ coefficients of the five 1250 cm^{-1} bands depend on the nanohoop size *n*, unlike those for linear oligo-paraphenylenes which are nearly independent from *n*.[47] The pressure coefficients for the low frequency modes are detailed in the supplementary material file.

The dependency of P_{oval}^{n} as a function of *n* is shown in Figure 5. The P_{oval}^{n} values become smaller for larger *n*. This very interesting trend is also reflected in the theoretical calculations which also predict a unique single P_{oval}^{n} with a rapid decrease with increasing, *n*. This gives strong support to our theoretical modeling of [n]CPPs under pressure and further justifies our confidence in the atomistic description obtained from theory presented in the next sections.

The deformations of the cross sections of CNTs under pressure are strongly diameter dependent, and tubes with larger diameter are softer (i.e., lower pressures are needed to induce the ovalization).[26,28,30,49] In Figure S9, we compare the ovalization pressures for SWCNTs with those of the [n]CPPs.[26,50] There is a parallel diameter dependence where P_{oval}^{n} decreases for larger diameters. In CNTs, this P_{oval}^{n} is related to the pressure at which deformation from circular to oval shape begins as modeled by the continuum theory of the buckling of elastic

rings.[51-54] By extrapolating this theory to [n]CPPs, as specified in the supplementary materials section, mechanical flexural rigidity can be deduced, which is equal to 0.57 ± 0.02 eV for [n]CPPs, in good agreement with the typical values of SWCNTs, ranging between 0.6 and 1.4 eV.[30,55] Moreover, one can estimate the bulk modulus of the [n]CPPs at pressures below P_{oval}^{n} obtaining values larger than those of SWCNTs (see Figure S9c).

3 Evolution of the structure with pressure. We now show detailed theoretical data from our high-pressure modeling of the [n]CPPs. First, we illustrate some of the shape changes due to pressure in Figure 6.

3A Energy and volume evolution of the unit cell with pressure. Figure 7 shows that, for all studied [n]CPPs, the relative total unit cell energy increases while the relative unit cell volume decreases with increasing pressure (details on XRD structures can be seen in Table S6 -S7 and Figure S10) . As expected, the volume decreases faster for larger [n]CPPs since they are less strained and thus less resistant to the deformation.

3B Ovalization and intramolecular torsions. One relevant structural feature of [n]CPPs is the distribution of conformations between neighboring benzene rings resulting from hydrogen-hydrogen steric repulsions forcing non-zero inter-phenyl torsions (θ) at room conditions (see insert in Figure 8a).[44] These torsional angles affect the degree of π-conjugation and quinonoidization in π–conjugated molecules, with torsional angles near co-planarity indicating greater aromatic character. Given the reduction of symmetry at higher pressures, we computed the average torsions between adjacent phenyls and use them as a geometrical index to monitor the molecular level transformation. For all [n]CPPs, torsions increase with increasing pressure as shown in Figure 8a. Since small [n]CPPs (n=5-7) are more strained than the larger congeners, their torsions increase very slowly during compression. Conversely, for larger [n]CPPs (n=8, 9, 10 and 12) the inter phenyl torsions increase rapidly up to ~4 GPa as seen in Figure 8a. Above 4 GPa, for [n]CPPs (n=8, 9, 10 and 12), the torsional angles slightly decrease or remain constant with compression, implying that further compression will induce different molecular rearrangements. Similar trends occur for the maximum torsion angles, θ_{max}, as shown in Figure S11. The flattening factor, f(P), conveniently measures the distortion from the approximately circular cross section:

$$f(P) = 1 - b(P)/a(P) \qquad (2)$$

where *a* and *b* are the major and minor molecular axis, respectively. We obtained *a* and *b* by measuring the longest and shortest carbon-carbon distances across the nanohoop. f(P) describes the deviation starting from a cylindrical shape at P=0.1 MPa to an oval (approximately ellipsoid) shape with increasing pressure, as shown in Figure 8b.

For small [n]CPPs (n=5-7), this remains below 10% when compressed up to 10 GPa, while for the rest of [n]CPPs it rises up to as high as 40 % within the same pressure range. As expected, and proved by our spectroscopic results, these flattening data show that smaller [n]CPPs are more rigid and resistant to ovalization. For medium size [n]CPPs, with n=8 and 9, f(P) plateaus between 5 GPa and 7 GPa, and then it increases. This trend reveals that [8]CPP and [9]CPP show some resistance to deformation up to a certain pressure limit, above which the structure of the molecule collapses acquiring a more oval shape. Above these pressures the ovalization becomes the dominant response in contrast to the behaviors of the smaller [5]- and [6]CPP, where the decrease of bond length alternation (BLA, as per equation (3)) toward quinonoid structures becomes the dominant geometry response to pressure as illustrated in Figure 6a. In other words, depending on the molecular size, the reduction of unit cell volume with increasing pressure is achieved by a reduction of the BLA in the smaller [n]CPPs and by a conformational plus flattening response in the larger ones. The modeling of the larger [n]CPPs (with n=10 and 12) show a slight decrease of f(P) at pressures up to 1 GPa, and then between 1 and 5 GPa, f(P) rises to around 20%. Therefore, the process of ovalization in large [n]CPPs is first primed by torsional accommodations in which one pair or two pairs of phenyl units rotate toward the tubular axis as illustrated in Figure 6b and 6c, respectively. Then, further increase of pressure causes ovalization, indicated by the increase of f(P).

3 C Aromaticity and high pressure. Aromaticity is directly affected by these various configurational changes, as measured by commonly used aromaticity indices including BLA, NICS and HOMA. BLA is defined as

$$BLA = \text{Average}(r + r_2 - r_1 - r'_1) \qquad (3)$$

Where r is the interring CC bond length r_1 and r'_1 are the adjacent bonds and r_2 is the following bond. This measure of aromaticity starts out with a large positive value of about 0.045 to 0.055 Å at ambient pressures depending on the size of the [n]CPP. (Smaller positive values indicate a somewhat quinonoid character where the interring bond length, r, is smaller

and so is r_2.) A decrease of the BLA is observed for n=5, 6, and 7 down to 0.02 to 0.04 Å upon 10 GPa pressure. The behavior of BLA for the n>7 members of the series is more complex with an increase of BLA and thereby an initial increase of the aromaticity due to the increased dihedral angles which leads to a disruption of inter-ring conjugation. Further compression then leads to a decrease of the BLA interpreted as a localization of the π-electrons in the highly ovalized CPP rings. The other aromaticity indices investigated are in line with the BLA index. For further discussion, see Figures S12 and S13 and the respective text in the SI.

4. Reversibility of pressure treatment. This subsection focuses on the reversibility of the deformation response to high pressures in [n]CPPs. Figure 9 contains the Raman spectra of [8]CPP before and after pressure treatment. Further data on the other [n]CPPs are shown in Figures S15, S18. In all cases the down stroke path was done in about four pressure steps of about 1.5 to 2.5 GPa each. The Raman spectra of the recovered samples after decompression are compared with the Raman spectra of the pristine samples before pressure treatment. We find very different reversibility behaviors for the different [n]CPPs. The Raman hysteresis between the pristine and recovered samples is given in Figures 10, S16, and S17 for the most intense bands. The trend is that the pressure cycling shows more reversibility for larger [n]CPPs compared to the least reversible small CPPs. Irreversibility of [5]- and [6]CPP comes from the formation of new σ-bonds leading to new phases with aggregation and polymerization of the CPP molecules that start to occur around 6 GPa. [21, 22] The Raman spectra of [n]CPPs shown in Figures S14 and S18 indicate that the spectra are irreversible after application of pressure for n=5, 6, and 8 while the spectra of [7]CPP, [9]CPP, [10]CPP, and [12]CPP are almost completely reversible in the pressure range studied. Since formation of new bonds are not predicted by the computer simulations for [n]CPPs with n>6 in the pressure range analyzed, it is natural to conclude that the structures of the remaining [n]CPPs are reversible and there are no permanent structural transformation resulting from the high pressure deformation. Figure 11a shows an example of reversible shape deformation of [10]CPP through ovalization. [7]CPP, [9]CPP, and [12]CPP also display similar structural reversibility. Therefore, the size of the [n]CPPs affects their pressure response in a way that the small rigid nanohoops reduce the strain energy by irreversible σ-bond formation. The larger and softer nanohoops undergo reversible ovalization as indicated by the spectroscopy and modeling. Similar σ-bond formation will likely occur also for the larger CPPs at even higher pressures.

We find that [8]CPP behaves differently than the rest of the [n]CPPs for n>6 both in the spectroscopy and in the modeling. For [8]CPP the p-RBM of the pristine sample (green in Figure 9) vanished upon pressure treatment. Simultaneously, two new features around 250 and 300 cm^{-1}, and a new very weak peak around 450 cm^{-1} (pink in Figure 9) emerge. Our vibrational calculation shows a new band at 447 cm^{-1} and very weak bands at 247 and 313 cm^{-1} (see Figure S18 for the recovered system). The experimental spectra also show two shoulders at 1200 and 1280 cm^{-1} only for the pristine samples which are also present in the calculation. Since the irreversible frequency shifts upon pressure for [8]CPP are small compared to those of [5]- and [6]CPP, we exclude the development of σ-bonds in [8]CPP. An alternative mechanism of irreversibility appeared in the modeling in terms of the evolution of the dihedral angles up to 90 degrees of two phenyl units as illustrated in Figure 11b. At pressures around P_{oval}^{n} the optimized geometry of [8]CPP contains a unique alignment where four benzene units represented in in Figure 8c in yellow (A) point towards the minor axis and four blue benzene units (Q) are distributed along the major axis (4A+4Q). This structure is denoted as Phase 1 is the ambient pressure XRD structure.[19] Detailed pressure dependence of the key structural parameters in the modelling of [8]CPP in a pressure increasing and releasing cycle with a maximum pressure of 10 GPa is shown in Figure S19.

However, above P_{oval}^{n}, a different conformation with an approximate distribution of 2A+6Q emerges as illustrated in Figure 11b. We denote the 4A+4Q conformation as Phase 1. This high-pressure conformation, shown also in Figure 11b, is denoted as Phase 2. When the pressure is released from above P_{oval}^{n}, the Phase 2 molecules keep their conformation and do not return to Phase 1. The explanation for such irreversibility is that the 2A+6Q conformer (Phase 2) has dihedral angles close to 90° resulting in a tighter intermolecular packing. The irreversibility of the Raman spectra of [8]CPP is thus due to the unique circumstance of the hindered rotation in Phase 2, a circumstance that is not present in the other [n]CPPs. We note that when P $\geq$ 8GPa, the molecules in Phase 2 have a smaller BLA and smaller torsion values indicating an overall more quinonoid structure compared to that in Phase 1. This phase remains stable up to at least the limit of the simulation at 10 GPa.

CONCLUSIONS

The combination of experimental Raman and DFT modeling of the molecular phases of [n]CPP nanohoop molecules under high pressure reveal unique trends in their shapes and electronic structures. Accordingly, for the larger [n]CPPs with $n\geq7$ the molecular phase

remains stable and there is no evidence for new intra- or intermolecular bond formation up to 10 GPa. The process of pressurization is reversible except for the special case of [8]CPP. Based on their elastic response to pressure, [n]CPPs can be qualitatively divided into two categories: rigid and soft. The group of rigid [n]CPPs includes [5]CPP[21], [6]CPP[22], and [7]CPP. These molecules display a stronger resistance to the pressure-induced deformations, which is related to their partially quinonoid structures. The soft [n]CPP group contains [8]CPP, [9]CPP, [10]CPP, and [12]CPP in which the molecules are more easily deformed into an oval shape, characterized by large torsions and flattening factors. In this work, [9]CPP, [10]CPP, and [12]CPP show significant cylindrical-to-oval deformations beyond the respective critical ovalization pressures.

The behavior of [8]CPP is between those of the "soft" and "rigid" nanohoops because its pattern of torsions among the benzene rings is unique and different from the other soft [n]CPPs. Two conformers were found in the geometry optimizations of [8]CPP. The conformation with large dihedral angles near 90° is reached at about 8 GPa. Computational modeling indicates that the structure is kinetically stuck in this hindered conformation when the external pressure is released. This provides a new mechanism of irreversibility during high pressure treatment of organic materials and this mechanism is well correlated with the experimental spectra.

A key confirmation of our modeling comes from the observation that there is a particular characteristic pressure for each [n]CPP where the change of pressure coefficients occurs. Based on the computations and experiments, we identify these critical pressure values, P_{oval}^{n}, as associated with the beginning of a significant degree of ovalization. The existence of a single P_{oval}^{n} value for each *n*, independent from the vibrational modes confirms the validity of our modeling of [n]CPPs under pressure. It reveals the fact that P_{oval}^{n} is associated with an intramolecular property of conformational origin and therefore affects more or less uniformly the whole molecule and consequently affects all their vibrational modes at the same ovalization pressure.

An additional general observation based on the trends found in this work for the [n]CPP series is that at high pressures in organic materials with herringbone packing, intermolecular σ-bond formation is hindered up to higher pressures than in the case of tubular packing. This is due to the larger intermolecular C···C contact distances in these herringbone structures, and

therefore higher pressures would be required to initiate the intermolecular bond formation. Encapsulation of guest molecules may affect this mechanism.

ASSOCIATED CONTENT

Supplementary information

The Supporting Information is available free of charge on the ACS Publications website. It contains: the Raman band assignments at ambient pressure, the S_1 and S_2 coefficients as a function of n for the 1250 cm^{-1} bands, ccomparison of G bands of [n]CPPs, SWCNTs and [n]LPPs, analysis of the Raman spectra as a function of pressure, [n]CPPs radial deformation modulus, crystal packing information, computed pressure dependent maximum torsions, aromaticity parameters as a function of pressure, aanalysis of the Raman spectra of the samples after decompression, and analysis of selected mode Grüneisen parameters.

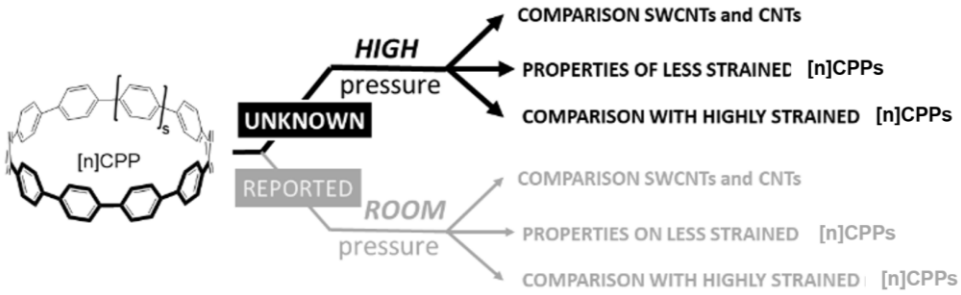

Figure 1. Chemical formula of [n]CPP nanohoops, n=5-12, in the context of the objectives of this research. n=s+9 is illustrated.

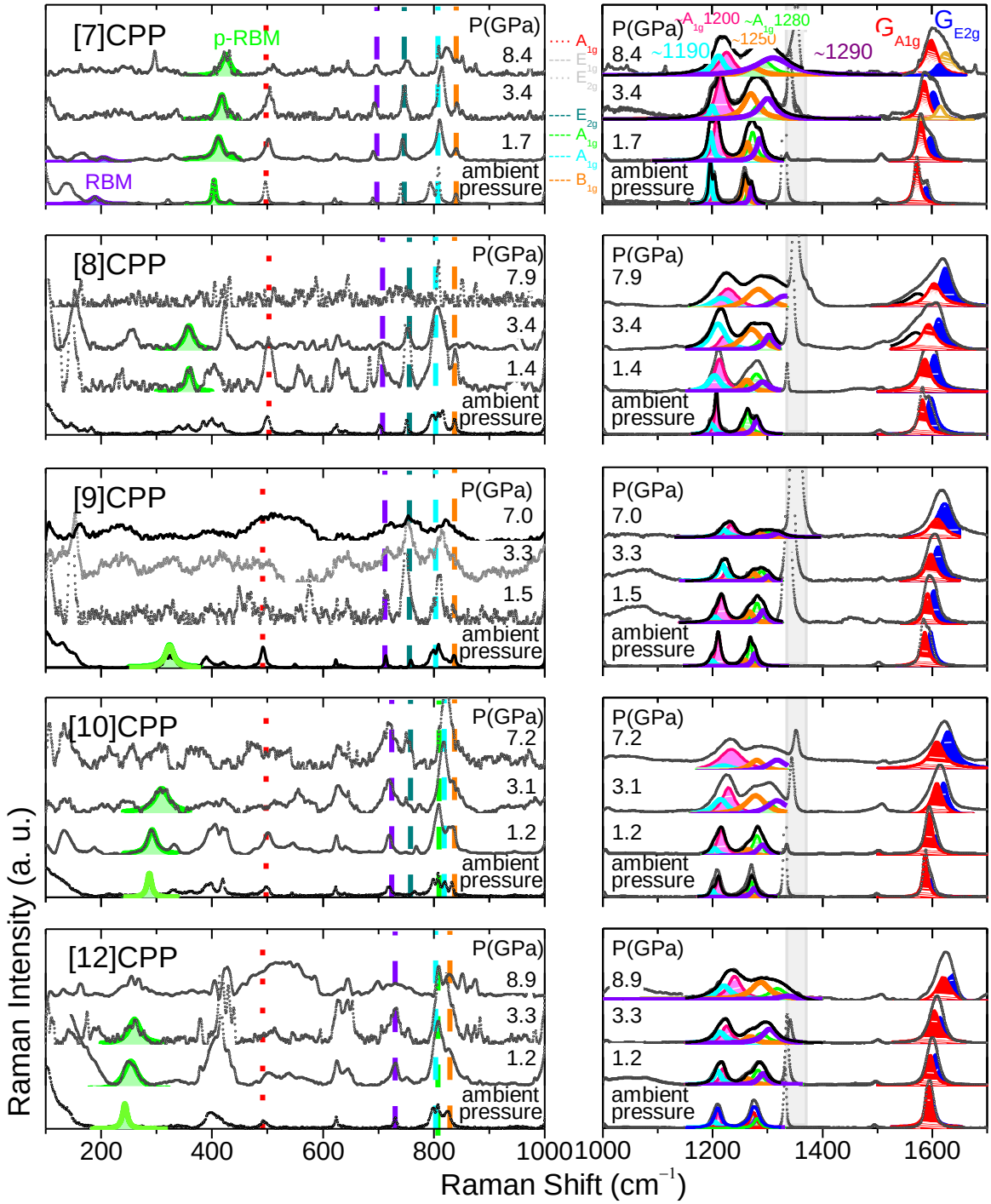

Figure 2. The experimental Raman spectra of [n]CPPs at selected pressures taken with the 785 nm excitation laser, increasing pressure from the bottom to the top. The left column corresponds to the low frequency region with peaks normalized to 1/5th of the intensities of the G bands. The right column corresponds to the high frequency region with intensities normalized to the G bands. The G_{A1g} and G_{E2g} contributions are shown in red and blue, respectively. Pink and green areas correspond to the 1200 and 1280 cm^{-1} bands, respectively. In the low frequency region the green areas indicate the p-RBM and the purple lines correspond to the RBM. The pressure calibrant band is in the gray region. Colored vertical dashed lines are used to denote different low intensity modes: red bar correspond to the Radial Flexural mode (RFM); grey, purple and dark green bars to the 610, 673 and 750 cm^{-1} E_{2g} modes, respectively; light green and light blue bars are used for the 973 cm^{-1} and 805 cm^{-1} A_{2g} modes; and the orange one to the E_{2g} at 836 cm^{-1}.

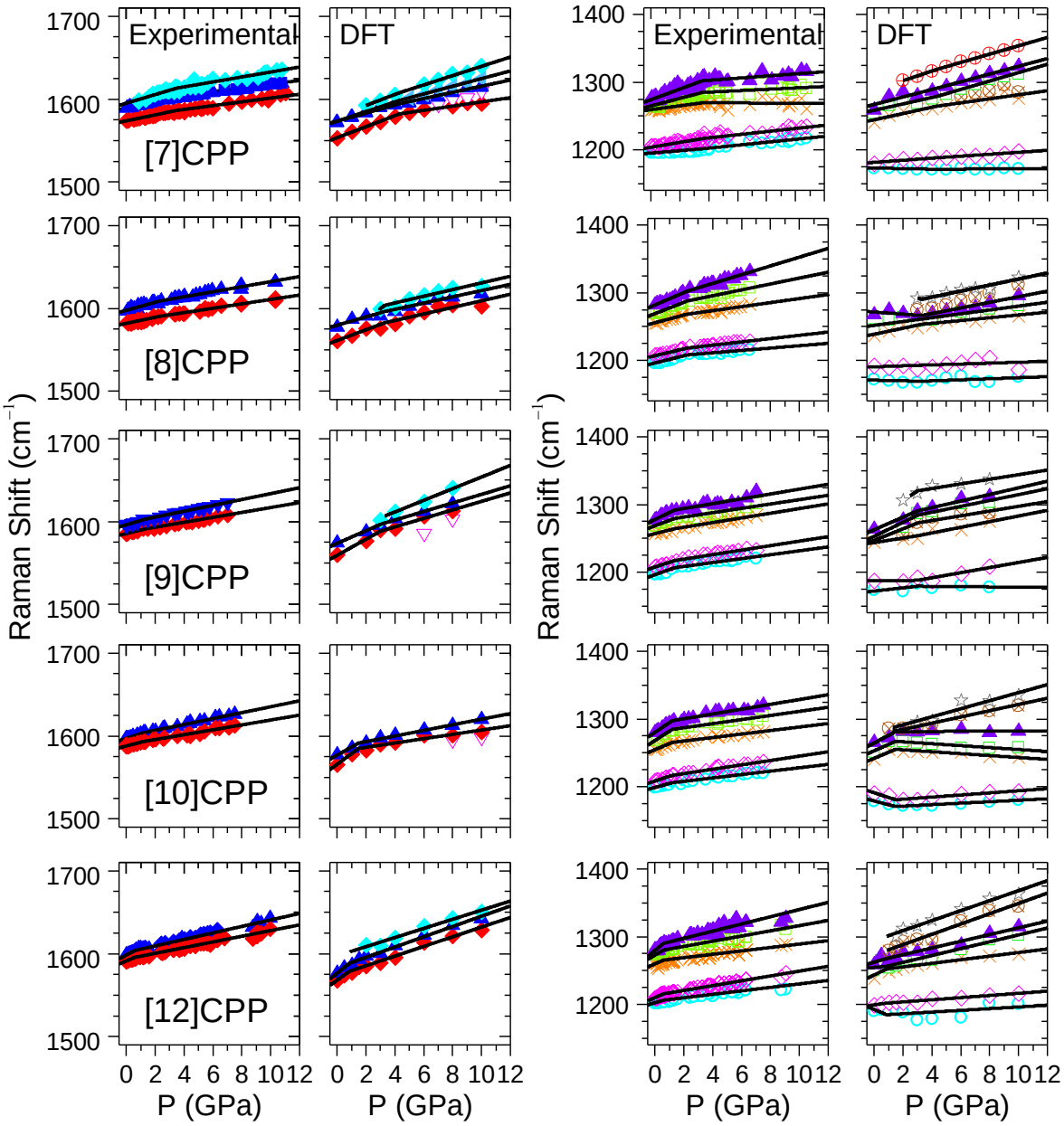

Figure 3. Pressure dependence of the Raman shifts in the 1200-1600 cm^{-1} region for the [n]CPPs. Experimental (the first and the third column) and the computed (the second and fourth column). Only the molecular phase data are presented as discussed. Red diamonds◇, correspond to the G_{A1g} band and blue triangles ▲ to the G_{E2g} band, cyan circles ○ 1190 cm^{-1} E_{2g}; pink diamonds ◇ 1200 cm^{-1} A_{1g}; orange crosses ×1250 cm^{-1} E_{2g}; green squares □ 1280 cm^{-1} A_{1g}; purple filled triangles▲ 1290 cm^{-1} E_{1g}. Solid lines correspond to the data fitting to eq. 1.

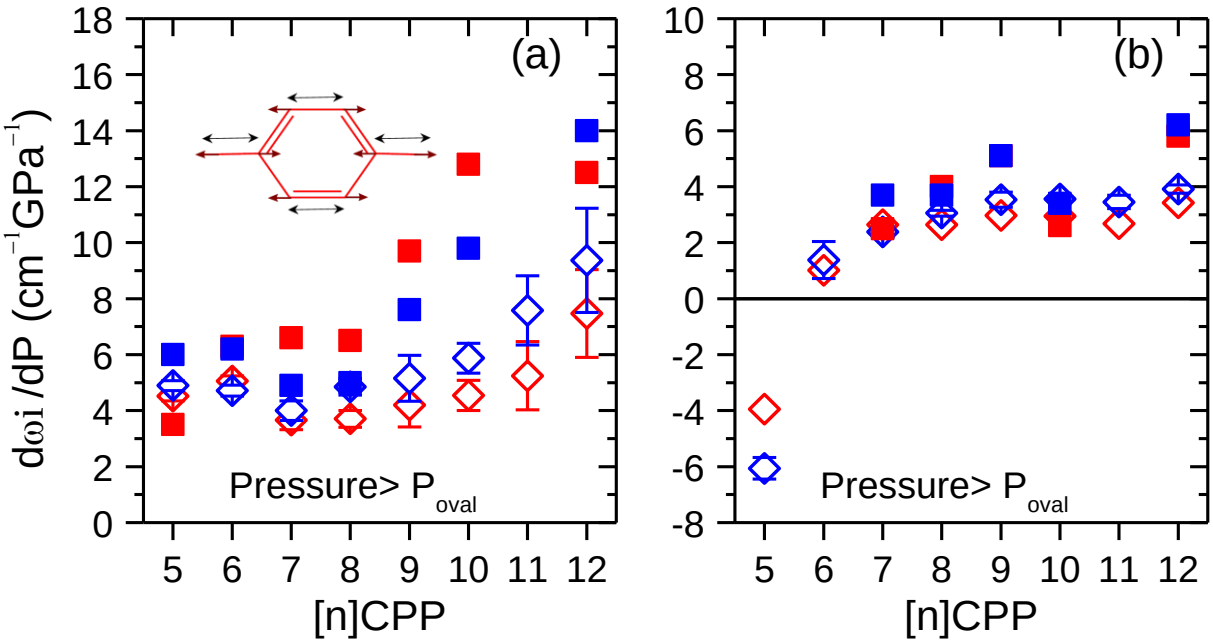

Figure 4. Diameter dependence of the pressure coefficients of the G_{E2g} (◇) and G_{A1g} (◇) modes for [5]- to [12]CPPs. (a) S_1, (b) S_2. Empty diamonds correspond to experimental results while filled squares to calculations. Data for [5]- and [6]CPP are taken from ref. 21 and 22.

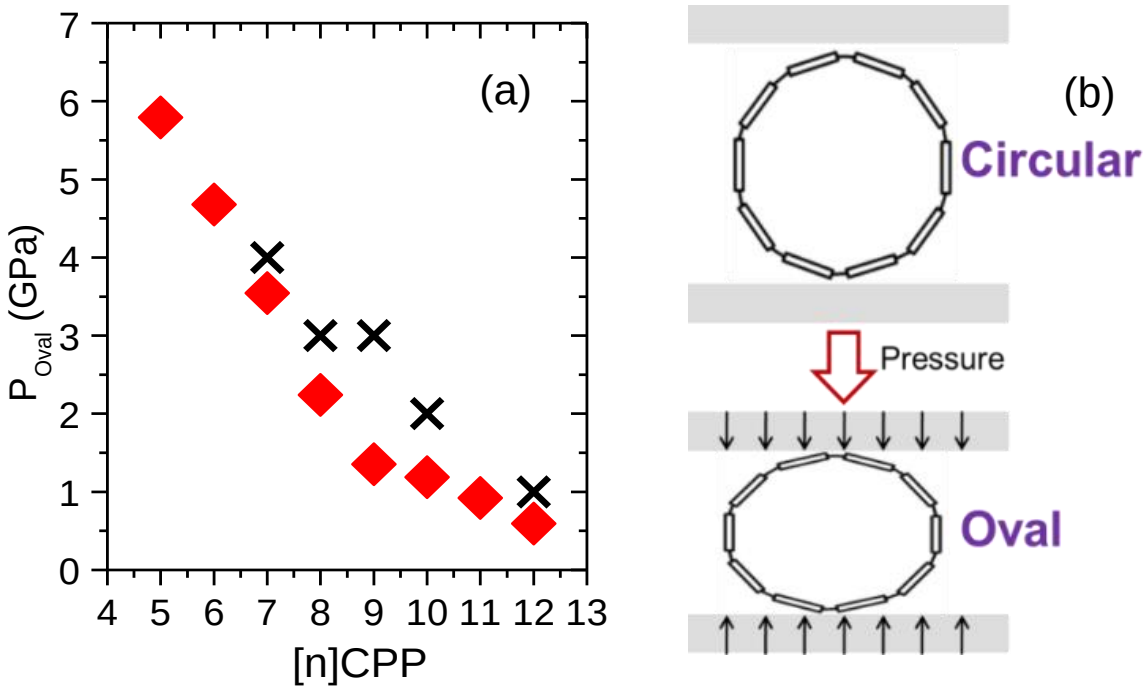

Figure 5. (a) Ovalization pressure as a function of diameter of the experimental:(◆) and theoretical (X) results obtained from the Raman shift as a function of pressure of the G bands and 1200 cm^{-1} bands. (b) Schematic representation of the pressure induced ovalization of [10]CPP. Note that the pressure is isotropic in both computations and experiments. Data for [5]- and [6]CPP are from ref. 21 and 22.

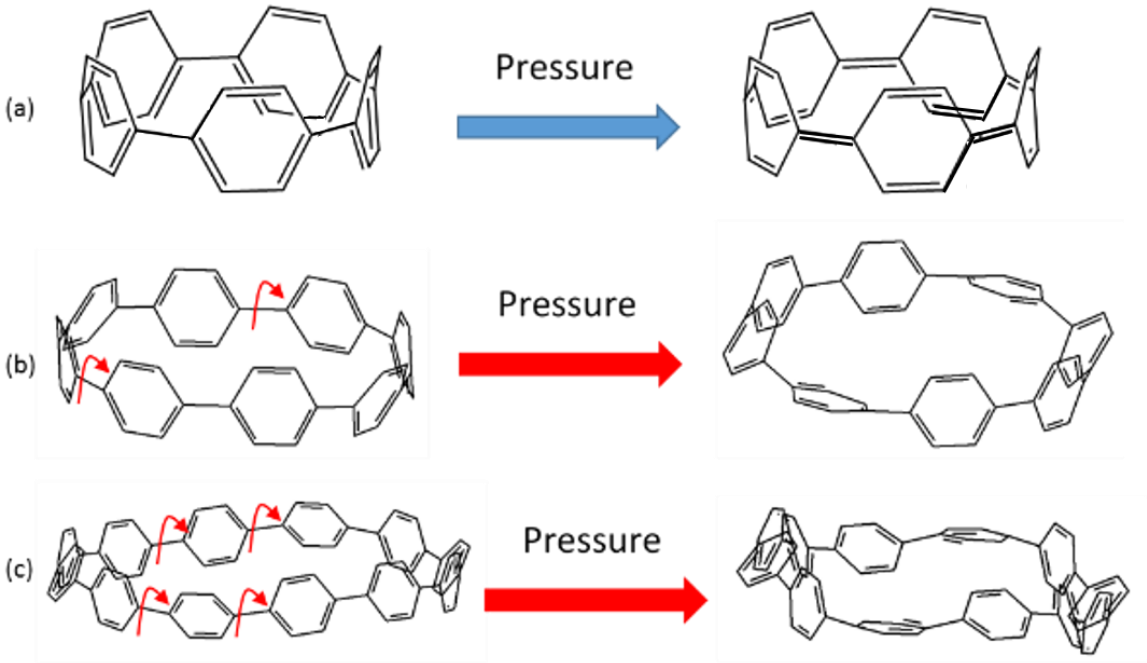

Figure 6. DFT optimized size-dependent compression behaviors of CPPs due to external pressure in the molecular phase. (a) The aromatic character of small CPPs changes to partially quinonoid; the n=5 case is illustrated. (b) In the larger [n]CPPs pairs of phenyl units rotate toward the axis. The case of n=8 is illustrated here showing one pair of such rotation. For n=9, 10 and 12 two pairs rotate as illustrated in (c).

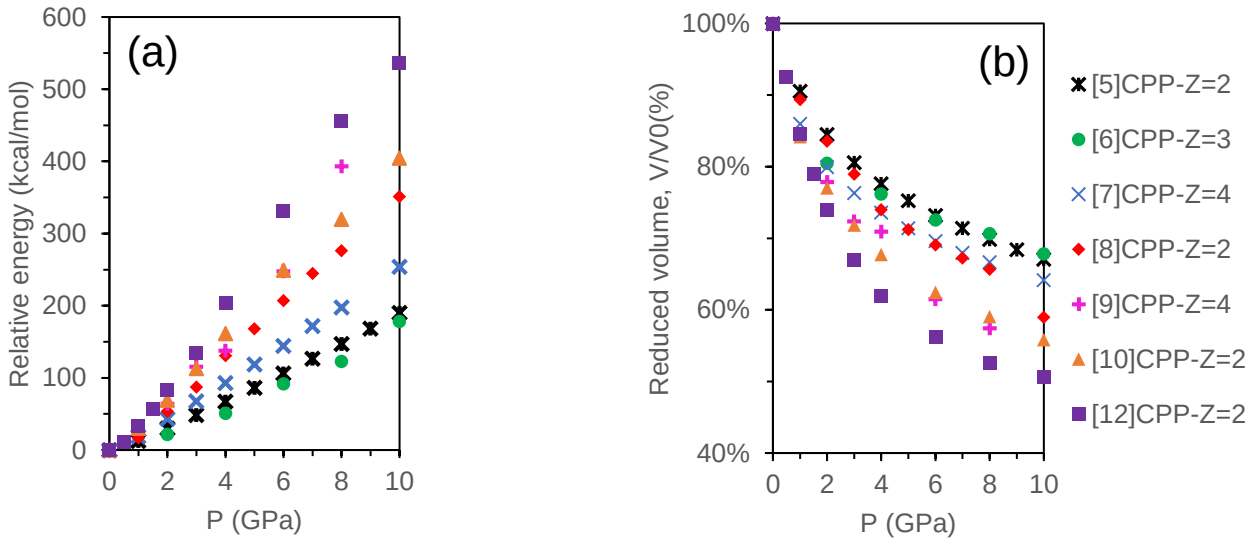

Figure 7. Computed pressure dependent energetics and volumes in the modeling of [n]CPPs (n=5~10 and 12). (a) Relative total energy per pair of molecules. (b) Percentage reduction of the unit cell volume with respect to the V_0 volume of each [n]CPP at P=0.

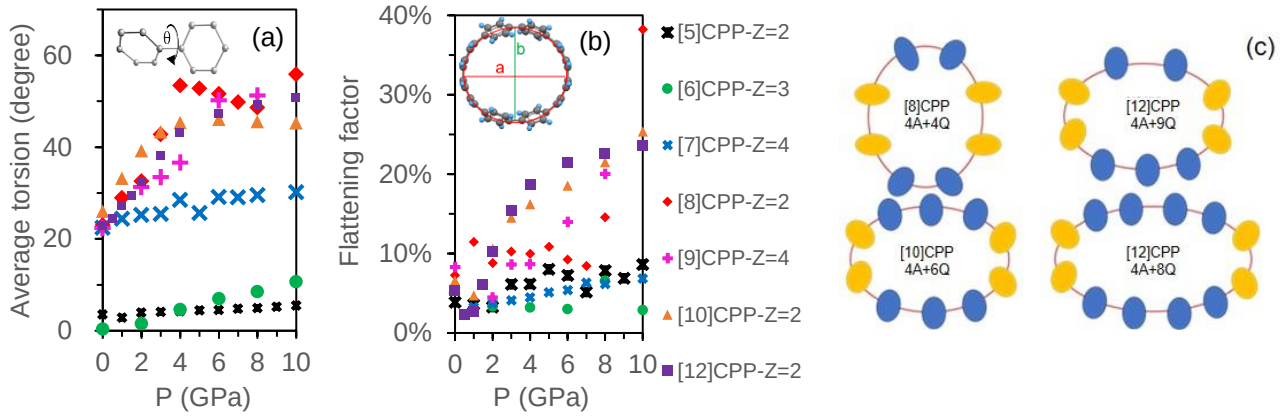

Figure 8. Geometrical parameters as a function of pressure obtained from the DFT optimized structures for [n]CPPs (n=5~10 and 12).(a) Average torsions (θ, inset shows and torsional angle (θ) between two neighboring phenyl units). (b) Flattening factors, *f,* inset shows the major and minor axis of [8]CPP a (red) and b (green), respectively. (c) DFT optimized phenyl alignments at P_{oval}^{n}. The blue filled ellipses represent quinonoid units (Q), and the yellow filled ellipses represent the more aromatic units (A).

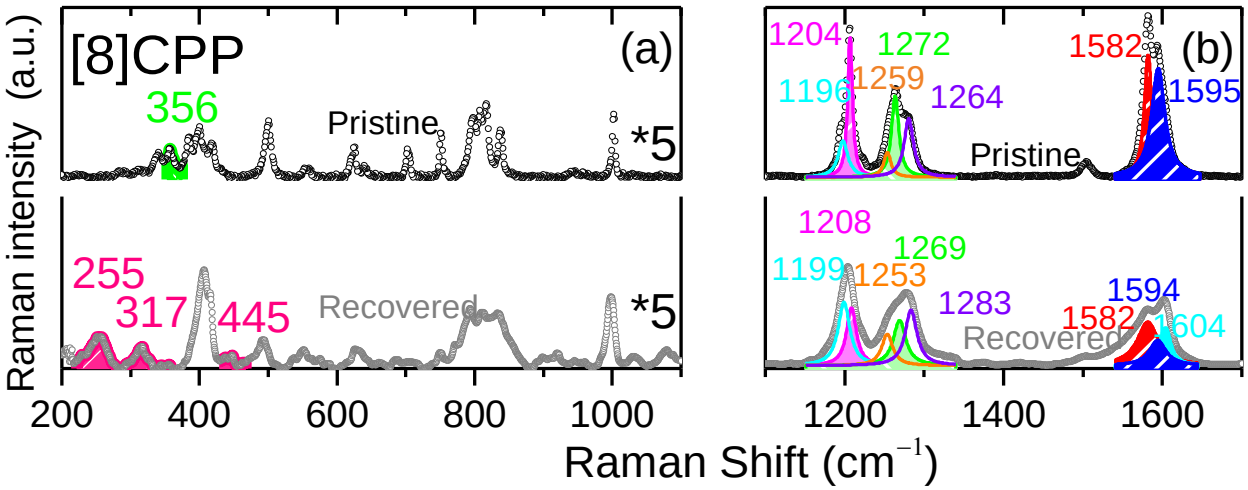

Figure 9. The experimental Raman spectra of [8]CPP before and after pressure treatment with maximum pressure of 11 GPa. (a) 200 – 1100 cm^{-1} and (b) 1100 – 1700 cm^{-1}.

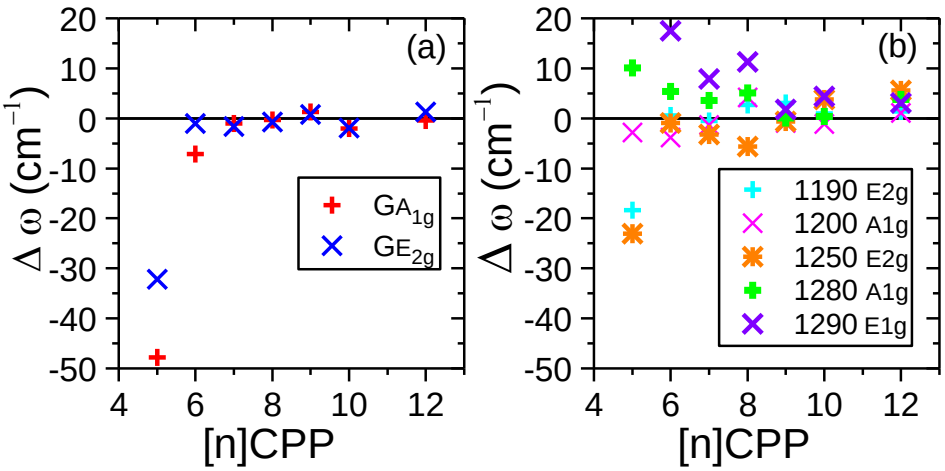

Figure 10. Experimental differences in the Raman shifts between the decompressed samples released from about 10 GPa to ambient pressure and the pristine sample. (a) G modes, and (b) five modes between 1170 and 1310 cm^{-1}.

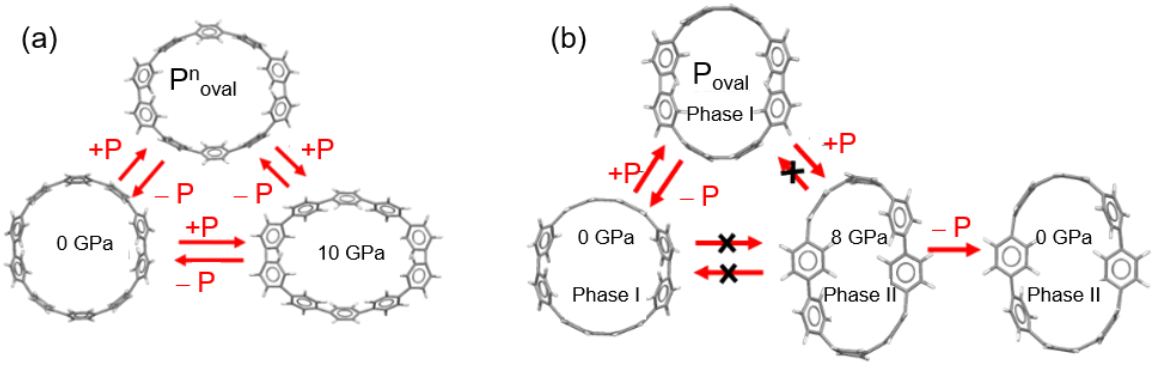

Figure 11. DFT optimized structures on pressure cycling. (a) Reversible for [10]CPP. (b) Irreversible for [8]CPP.

Methods

Experimental section: [7]- to [12]CPP. [n]CPPs with n = 8, 9, 10, 11, and 12 were provided by Yamago et al., and were synthesized by using a synthetic strategy through multinuclear arylplatinum complexes. [7]CPP was provided by Jasti et al., synthesized through Suzuki – Miyaural cross-coupling/ macrocyclization to generate macrocycles and their consecutive reduction routes. [15] Raman measurements at ambient and approximately hydrostatic high pressure conditions were conducted with a Senterra dispersive Raman spectrometer from Bruker with a 785 nm excitation wavelength with a standard spectral resolution of 3 cm^{-1}. Pressure studies were conducted in a sapphire anvil cell (SAC) with anvils of a diameter culet of 380 μm. Pressures up to 12 GPa were reached, although for each [n]CPP the maximum pressure achieved was slightly different. No pressure transmitting medium was used and diamond chips were employed as pressure calibrant. [56]

For all Raman spectra the background has been removed, setting the baseline at zero before any further spectral analysis is done. Second derivative analyses of the spectra have been done to obtain the maxima. These maxima are used as initial values of the fitting with a sum of Lorentzian curves, as reported elsewhere,[57] and where the full width half maximum (FWHMs) ranges between 8 and 40 cm^{-1}. We consider the areas of the bands as the measured intensities.

II.2 Computational modeling*:* The Density Functional Theory (DFT) based crystal modeling is based on the Quantum Espresso (QE) package[58, 59] that includes hydrostatic (isotropic) pressure as an explicit input parameter. We used PBE[58,59]as the density functional combined with the Rappe-Rabe-Kaxiras-Joannopoulos ultrasoft pseudopotential[60, 61] and a plane wave basis set with a 47 Ry cutoff. For each pressure between 0 and 10 GPa, we performed full geometry optimizations using the default convergence criteria. With the optimized geometries obtained at each P value, we calculated the vibrational frequencies at the frozen geometries with the Gaussian 09 package.[62] For the theoretical vibrational spectra, we used the B3LYP/6-31G(d) model chemistry with non-resonant Raman intensities. A uniform scaling factor of 0.95 was used for all calculated frequencies.

Tables S1 and S2 include the unit cell parameters, packing type, and molecular structure parameters obtained both from the single X-ray diffraction and the optimized geometries for all [n]CPPs we investigated. Good agreements between the experiments and our computations provide the basis for the presented modeling under high pressure.

Acknowledgements

We thank Dr. Paula Mayorga Burrezo for her help running the experiments. We thank Prof. Yamago et al. and Prof. R. Jasti for providing the samples. We thank the U. S. National Science Foundation for its support of this research at Georgetown University (grant number CHE-1006702). Financial support from MINECO, Government of Spain is acknowledged (project reference FEDER CTQ2015-69391-P). This work has been also supported by MINECO through the projects CSD2007-00045, CTQ2012-38599-C02-02 and CTQ2013-48252-P. MPA is grateful to the Spanish Ministerio de Educación, Cultura y Deporte for an FPU grant. M.P.-A. would like to acknowledge the support of the European Research Council (ERC) Grant "Hecate" Reference No. 695527.

Author contributions

MPA, VGA and MT conducted the experiments and the analysis. MPA conceived and designed the project. MK and LQ conducted the computational work. MPA, LQ, MK and JC wrote the paper.

Author Information

Reprints and permissions information is available at the web. The authors declare no competing financial interest. Readers are welcome to comment on the online version of the paper. Correspondence and requests form materials should be addressed to MP, LQ, MK or JC.

References

1. Nicol, M., Yin, G.Z. Organic chemistry at high pressure: Can unsaturated bonds survive 10 GPa? *J. de Physique Coll*. **1984**, *45*, C8-163-C8-172.

2. Aguiar, A. L., Capaz, R. B., Filho, A. G. S., San-Miguel, A. Structural and Phonon Properties of Bundled Single- and Double-Wall Carbon Nanotubes Under Pressure, *J. Phys. Chem. C.* **2012**, *116*, 22637-22655.

3. Imtani, A. N., Jindal, V. K. *Comput. Mater.* Structure of chiral single-walled carbon nanotubes under hydrostatic pressure. *Sci.* **2009**, *46*, 297-302.

4. Wen, X.D., Hoffmann, R., Ashcroft, N.W. Benzene under high pressure: a story of molecular crystals transforming to saturated networks, with a possible intermediate metallic phase. *J. Am. Chem. Soc*. **2011**, *133(23)*, 9023-9035.

5. Chen, B., Hoffmann, R., Ashcroft, N. W., Badding, J. V., Xu, E.-S., Crespi, V. H. Linearly polymerized benzene arrays as intermediates, tracing pathways to carbon nanothreads. *J. Am. Chem. Soc*. **2015**, *137*, 14373–14386.

6. Fitzgibbons, T. C., Guthrie, M., Xu, E.-S., Crespi, V. H., Davidowski, S. K., Cody, G. D., Alem, N., Badding, J. V. Benzene-derived carbon nanothreads. *Nat. Mater*. **2015**, *14*, 43–47.

7. Heimel, G., Hummer, K., Ambrosch-Draxl, C., Chunwachirasiri, W., Winokur, M. J., Hanfland, M., Oehzelt, M., Aichholzer, A., Resel, R. Phase transition and electronic properties of fluorene: A joint experimental and theoretical high-pressure study. *Phys. Rev. B*, **2006**, *73*, 024109.

8. Casati, N., Kleppe, A., Jephcoat, A.P., Macchi, P. Putting pressure on aromaticity along with in situ experimental electron density of a molecular crystal. *Nature comm*. **2016**, *7*, 10901.

9. Kayahara, E., Kumar Patel, V., Yamago, S., Synthesis and characterization of [5] cycloparaphenylene. , *J. Am. Chem. Soc*. **2014**, *136(6)*, 2284-2287.

10. Gonzalez-Veloso, I., Cabaleiro-Lago, E. M., Rodriguez-Otero, J. Fullerene size controls the selective complexation of [11] CPP with pristine and endohedral fullerenes. *Phys.Chem.Chem.Phys.* **2018**, *20*, 11347-11358.

11. Rio J., Beeck S., Rotas, G., Ahles, S., Jacquemin, D., Tagmatarchis N., Ewels, C., Wegner H. A. Electronic Communication between two [10]cycloparaphenylenes and Bis(azafullerene) (C59N)2 Induced by Cooperative Complexation. *Int. Ed. Angew. Chem.* **2018**, 10.1002/anie.201713197.

12. Dresselhaus, M., Dresselhaus, G., Avouris, P. *Carbon Nanotubes: Synthesis Properties, Applications;* Springer, Berlin, **2001**.

13. Reche-Tamayo, M., Pérez-Guardiola, A., J.Pérez-Jiménez, A., Sancho-García, J. C. Reactivity of cycloparaphenylenes: Studying the possible growth of single-walled carbon nanotubes with DFT methods. *Chem. Phys. Let*. 2018, 697, 17-22.

14. Ajayan, P. M**.** Nanotubes from carbon. *Chem. Rev*. **1999**, *99*, 1787-1800.

15. Xia J., Jasti R. Synthesis, characterization, and crystal structure of [6] cycloparaphenylene, *Angew. Chem. Int. Ed.* **2012,** *51*, 2474 –2476.

16. Jasti, R., Bhattacharjee, J., Neaton, J. B., Bertozzi, C. R. Synthesis, characterization, and theory of [9]-,[12]-, and [18] cycloparaphenylene: carbon nanohoop structures. *J. Am. Chem. Soc*. **2008**, *130*, 17646-17647.

17. Sisto, T. J., Golder, M. R., Hirst, E. S., Jasti, R. Selective synthesis of strained [7] cycloparaphenylene: an orange-emitting fluorophore. *J. Am. Chem. Soc*. **2011**, *133*, 15800-15802.

18. Takaba, H., Omachi, H., Yamamoto, Y., Bouffard, J., Itami, K. Selective synthesis of [12] cycloparaphenylene. *Angew. Chem., Int. Ed*. **2009**, *48*, 6112-6116.

19. Yamago, S., Watanabe, Y., Iwamoto, T. Synthesis of [8] cycloparaphenylene from a square-shaped tetranuclear platinum complex, *Angew. Chem., Int. Ed*. **2010**, *49*, 767-771.

20. Nishihara, T., Segawa, Y., Itami, K., Kanemitsu, Y. Synthesis of [8] cycloparaphenylene from a square-shaped tetranuclear platinum complex. *J. Phys. Chem. Lett.* **2012**, *3*, 3125−3128.

21. Qiu, L., Peña-Alvarez, M., Taravillo, M., Evans, P. J., Darzi, E. R., Jasti, R., Mayorga Burrezo, P., López Navarrete, J. T., Baonza, V. G., Casado, J., Kertesz, M. High-Pressure Chemistry and the Mechanochemical Polymerization of [5]-Cyclo-p-phenylene**.** *Chem. Eur. J.* **2017**, *23*, 16593-16604

22. Qiu, L., Peña-Alvarez, M., Taravillo, M., Baonza, V. G., Casado J., Kertesz, M. Mechanochemistry in [6] Cycloparaphenylene: A Combined Raman Spectroscopy and Density Functional Theory Study**.** *ChemPhysChem*, **2018**, *19*, 103-1916..

23. Zannoni, G., Zerbi, G. Lattice dynamics and vibrational spectra of undoped and doped polyparaphenylene**.** *J. Chem. Phys*. **1985**, *82*, 31-38.

24. Lu, J. P. Elastic properties of carbon nanotubes and nanoropes. *Phys. Rev. Lett*. **1997**, *79*, 1297-1300.

25. Meo, M., Rossi, M. Prediction of Young's modulus of single wall carbon nanotubes by molecular-mechanics based finite element modelling. *Comp. Sci. Tech.* **2006**, *66*, 1597-1605.

26. Sun, D. Y., Shu, D. J., Ji, M., Liu, F., Wang, M., Gong, X. G. Pressure-induced hard-to-soft transition of a single carbon nanotube**.** *Phys. Rev. B* **2004**, *70*, 165417.

27. Zhang, C., Bet, S K., Lee, S. S., Sun Z., Mirri, F., Colvin V. L., Yakobson B. I., Tour J. M., Hauge R. H. Closed-edged graphene nanoribbons from large-diameter collapsed nanotubes. *ACS Nano* **2012**, *6*, 6023–6032.

28. Shen, Y., Zerulla D. Dynamics of the radial deformation recovery process of single-wall carbon nanotubes**.** *Carbon*, **2018,** *132* 466–476.

29. R. S. Ruoff, J. Tersoff, D. C. Lorents, S. Subramoney, B. Chan, Radial deformation of carbon nanotubes by van der Waals forces**.** *Nature* (London) **1993**, *364*, 514-516.

30. Elliott, J. A., Sandler, J. K. W., Windle, A. H., Young, R. J., Shaffer, M. S. P. Collapse of single-wall carbon nanotubes is diameter dependent. *Phys. Rev. Lett*. **2004,** *92*, 095501.

31 .Cerqueira, F. T. T., Silvana, B., San-Miguel, A., Marques, M. A. L**.** Density-functional tight-binding study of the collapse of carbon nanotubes under hydrostatic pressure. *Carbon* **2014**, *69*, 355–360.

32. Chen, D., Sasaki, T., Tang, J., Qin, L. C. Effects of deformation on the electronic structure of a single-walled carbon nanotube bundle**.** *Phys. Rev. B* **2008**, 77, 125412.

33. Nishidate, K., Hasegawa, M. Universal band gap modulation by radial deformation in semiconductor single-walled carbon nanotubes**.** *Phys. Rev. B* **2008,** *78*, 195403.

34. Nishidate, K., Hasegawa, M. Deformation and transfer doping of a single-walled carbon nanotube adsorbed on metallic substrates. *Phys. Rev. B* **2010**, *81*, 125414.

35. Lourie, O., Wagner, H. D. Evaluation of Young's modulus of carbon nanotubes by micro-Raman spectroscopy, *J. Mat Research***, 1998**, *13*, 2418-2422**.**

36. Thostenson, E. T., Ren, Z., Chou, T. W. Advances in the science and technology of carbon nanotubes and their composites: a review. *Composites Sci. Technol.* **2001**, *13*, 1899-1912.

37. Ghandour, A. J., Crowe, I. F., Proctor, J. E., Sun, Y. W., Halsall, M.P., Hernandez, I., Sapelkin, A., Dunstan, D. J. Pressure coefficients of Raman modes of carbon nanotubes resolved by chirality: Environmental effect on graphene sheet**.** *Phys. Rev. B*. **2013,** *87*, 085416.

38. Peters, M. J., McNeil, L. E., Lu, J. P., Kahn, D. Structural phase transition in carbon nanotube bundles under pressure. *Phys. Rev. B* **2000**, *61*, 5939–5944.

39. Ling, C. C., Xue, Q. Z., Chu, L. Y., Jing, N. N., Zhou, X. Y. Radial collapse of carbon nanotubes without and with Stone–Wales defects under hydrostatic pressure, *RSC Adv*. **2012**, *2*, 12182–12189.

40. Yao, M., Wang, Z., Liu, B., Zou, Y., Yu, S., Lin, W., Hou, Y., Pan, S., Jin, M., Zou, B, Cui, T., Zou, G., Sundqvist, B. Raman signature to identify the structural transition of single-wall carbon nanotubes under high pressure**.** *Phys. Rev. B* **2008**, *78*, 205411.

41. Venkateswaran, U. D., Rao, A. M., Richter, E., Menon, M., Rinzler, A., Smalley, R. E., Eklund, P. C. Probing the single-wall carbon nanotube bundle: Raman scattering under high pressure. *Phys. Rev. B* **1999**, *59*, 10928–10934.

42. Wu, G., Yang, X., Dong, Radial breathinglike mode of the collapsed single-walled carbon nanotube bundle under hydrostatic pressure. *Appl. Phys. Lett*. **2006**, *88*, 223114.

43. Peña Alvarez M., Burrezo, P. M., Kertesz, M., Iwamoto, T., Yamago, S., Xia, J., Jasti, R., López Navarrete, J. T., Taravillo, M., Baonza, V. G., Casado, J. Properties of Sizeable [n]Cycloparaphenylenes as Molecular Models of Single-Wall Carbon Nanotubes Elucidated by Raman Spectroscopy: Structural and Electron-Transfer Responses under Mechanical Stress. *Angew. Chem. Int*. Ed. **2014**, 53, 7033-7037.

44. Peña Alvarez, M., Qiu, L., Taravillo, M., Baonza, V. G., Ruiz Delgado, M. C., Yamago, S., Jasti, R., López Navarrete, J. T., Casado, J., Kertesz, M. From linear to cyclic oligoparaphenylenes: electronic and molecular changes traced in the vibrational Raman spectra and reformulation of the bond length alternation pattern. *Phys. Chem. Chem. Phys.* **2016**, ***18***, 11683-11692.

45. Sandler, J., Shaffer, M. S. P., Windle, A. H. Variations in the Raman peak shift as a function of hydrostatic pressure for various carbon nanostructures: A simple geometric effect. *Phys. Rev. B* **2003**, *67*, 035417.

46. Hanfland, M., Brillante, A., Syassen, K., Stamm, M., Fink, J. Polyparaphenylene under pressure: Optical absorption and vibrational modes. *J. Chem. Phys.* **1989**, *90* (3), 1930–1934.

47. Martin, C. M., Cai, Q., Guha, S., Graupner, W., Chandrasekhar, M., Chandrasekhar, H. R. Raman modes in oligophenyls under hydrostatic pressure. *Phys. Stat. Sol.* **2004**, *241*, 3339−3344.

48. Guha, S., Graupner, W., Resel, R., Chandrasekhar, M., Chandrasekhar, H. R., Glaser, R., Leising, G. Tuning Intermolecular Interactions: A Study of the Structural and Vibrational Properties of p-Hexaphenyl under Pressure**.** *J. Phys. Chem. A* **2001**, *105* (25), 6203-6211.

49. Hasegawa, M., Nishidate, K. Radial deformation and stability of single-wall carbon nanotubes under hydrostatic pressure**.** *Phys. Rev. B* **2006**, *74*, 115401.

50. Chang, T. Explicit solution of the radial breathing mode frequency of single-walled carbon nanotubes. *Acta. Mech. Sinica* 2007, 23, 159–162.

51. Levy, M. Theory of Elastic Stability. *J. Math. Ser*. **1884**, *3*, 7.

52. Carrier, G. F. On the buckling of elastic rings. *J. Math. Phys*. **1947**, *26*, 94–103.

53. Chaskalovic, J., Naili, S. Bifurcation theory applied to buckling states of a cylindrical shell. *Angew. Math. Phys*. **1995**, *46*, 149–155.

54. Landau, L. D., Lifshitz, E. M. *Elasticity Theory*, translated by J. B. Sykes, W. H. Reid, Pergamon Press, Oxford, 1**975**.

55. Yakobson, B. I., Brabec, C. J., Bernholc, H. Nanomechanics of Carbon Tubes: Instabilities beyond Linear Response. J. *Phys. Rev. Lett*. **1996**, *76*, 2511–2514.
56. Baonza, V. G., Taravillo, M., Arencibia, A., Cáceres, M., Núñez, J. Diamond as pressure sensor in high-pressure Raman spectroscopy using sapphire and other gem anvil cells**.** *J. Raman Spectrosc*. **2003**, *34*, 264-270.
57. Del Corro, E., Taravillo, M., González J., Baonza V. G. Raman characterization of carbon materials under non-hydrostatic conditions. *Carbon* **2011**, *49*, 973-979.
58. Paier, J., Hirschl, R., Marsman, M. Kresse, G, The Perdew–Burke–Ernzerhof exchange-correlation functional applied to the G2-1 test set using a plane-wave basis set**.** *J. Chem. Phys*. **2005**,*122,* 234102.
59. Giannozzi, P., Baroni, S., Bonini, N., Calandra, M., Car, R., Cavazzoni, C., Ceresoli, D., Chiarotti, G. L., Cococcioni, M., Dabo, I., Dal Corso, A., Fabris, S., Fratesi, G., de Gironcoli, S., Gebauer, R., Gerstmann, U., Gougoussis, C., Kokalj, A., Lazzeri, M., Martin-Samos, L., Marzari, N., Mauri, F., Mazzarello, R., Paolini, S., Pasquarello, A., Paulatto, L., Sbraccia, C., Scandolo, S., Sclauzero, G., Seitsonen, A. P., Smogunov, A., Umari, P., Wentzcovitch, R. M. QUANTUM ESPRESSO: a modular and open-source software project for quantum simulations of materials**.** *J. Phys. Condens. Matter*, **2009**, *21*, 395502.
60. We used the pseudopotentials C.pbe-n-rrjkus_psl.UPF and H.pbe-rrkjus_psl.UPF from the Quantum Espresso pseudopotential data base: http://www.quantum-espresso.org/pseudopotentials.
61. Rappe, A. M., Rabe, K. M., Kaxiras, E., Joannopoulos, J. D., Erratum: Optimized pseudopotentials *Phys. Rev. B*, **1990,** *41*, 1227. *Phys. Rev. B*, 44, 13175.
62. Gaussian 16, Frisch, M. J., Trucks, G. W., Schlegel, H. B., Scuseria, G. E., Robb, M. A., Cheeseman, J. R., Scalmani, G., Barone, V., Mennucci,B., Petersson,G.A., Nakatsuji,H., Caricato,M., Li, X., Hratchian, H. P., Izmaylov, A. F., Bloino, J., Zheng, G., Sonnenberg, J. L., Hada, M., Ehara, M., Toyota, K., Fukuda, R., Hasegawa, J., Ishida, M., Nakajima, T., Honda, Y., Kitao, O., Nakai, H., Vreven, T., Montgomery, J. A., Jr., Peralta, J. E., Ogliaro, F., Bearpark, M., Heyd, J. J., Brothers, E., Kudin, K.N., Staroverov, V. N., Kobayashi, R., Normand, J., Raghavachari, K., Rendell, A., Burant, J. C., Iyengar, S. S., Tomasi, J., Cossi, M., Rega, N., Millam, J. M., Klene, M., Knox, J. E., Cross, J. B., Bakken, V., Adamo, C., Jaramillo, J., Gomperts, R., Stratmann, R.E., Yazyev, O., Austin, A. J., Cammi, R., Pomelli, C., Ochterski, J. W., Martin, R.L., Morokuma, K., Zakrzewski, V. G., Voth, G. A., Salvador, P., Dannenberg, J. J., Dapprich, S., Daniels, A. D., Farkas, O., Foresman, J. B., Ortiz, J. V., Cioslowski, J., Fox, D. J. Gaussian, Inc., Wallingford CT, 2016.

TOC

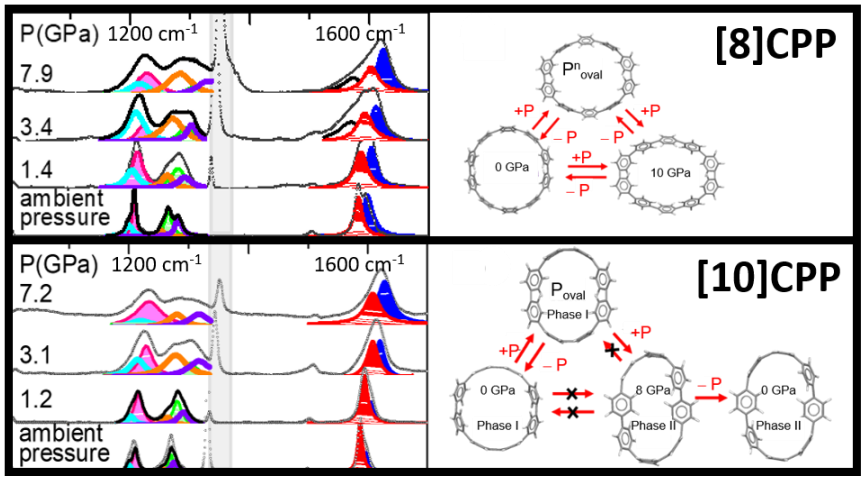
P(GPa)
1200 cm-1
1600 cm-1
7.9
3.4
1.4
ambient pressure
[8]CPP
Pnoval
+P
– P
0 GPa
10 GPa
P(GPa)
1200 cm-1
1600 cm-1
7.2
3.1
1.2
ambient pressure
[10]CPP
Poval
Phase I
0 GPa
Phase I
8 GPa
Phase II
0 GPa
Phase II